

# *Linking atmospheric rivers and warm conveyor belt airflows*

Article

Published Version

Creative Commons: Attribution 4.0 (CC-BY)

Open access

Dacre, H. F. ORCID: <https://orcid.org/0000-0003-4328-9126>,  
Martinez-Alvarado, O. ORCID: <https://orcid.org/0000-0002-5285-0379> and Mbengue, C. O. (2019) Linking atmospheric rivers and warm conveyor belt airflows. *Journal of Hydrometeorology*, 20 (6). pp. 1183-1196. ISSN 1525-7541  
doi: <https://doi.org/10.1175/JHM-D-18-0175.1> Available at <https://centaur.reading.ac.uk/83279/>

It is advisable to refer to the publisher's version if you intend to cite from the work. See [Guidance on citing](#).

To link to this article DOI: <http://dx.doi.org/10.1175/JHM-D-18-0175.1>

Publisher: American Meteorological Society

All outputs in CentAUR are protected by Intellectual Property Rights law, including copyright law. Copyright and IPR is retained by the creators or other copyright holders. Terms and conditions for use of this material are defined in the [End User Agreement](#).

[www.reading.ac.uk/centaur](http://www.reading.ac.uk/centaur)

**CentAUR**

Central Archive at the University of Reading

Reading's research outputs online

## Linking Atmospheric Rivers and Warm Conveyor Belt Airflows

H. F. DACRE

*Department of Meteorology, University of Reading, Reading, United Kingdom*

O. MARTÍNEZ-ALVARADO

*National Centre for Atmospheric Sciences, Reading, United Kingdom*

C. O. MBENGUE

*Department of Atmospheric, Oceanic and Planetary Physics, University of Oxford, Oxford, United Kingdom*

(Manuscript received 16 August 2018, in final form 31 March 2019)

### ABSTRACT

Extreme precipitation associated with extratropical cyclones can lead to flooding if cyclones track over land. However, the dynamical mechanisms by which moist air is transported into cyclones is poorly understood. In this paper we analyze airflows within a climatology of cyclones in order to understand how cyclones redistribute moisture stored in the atmosphere. This analysis shows that within a cyclone's warm sector the cyclone-relative airflow is rearwards relative to the cyclone propagation direction. This low-level airflow (termed the feeder airstream) slows down when it reaches the cold front, resulting in moisture flux convergence and the formation of a band of high moisture content. One branch of the feeder airstream turns toward the cyclone center, supplying moisture to the base of the warm conveyor belt where it ascends and precipitation forms. The other branch turns away from the cyclone center exporting moisture from the cyclone. As the cyclone travels, this export results in a filament of high moisture content marking the track of the cyclone (often used to identify atmospheric rivers). We find that both cyclone precipitation and water vapor transport increase when moisture in the feeder airstream increases, thus explaining the link between atmospheric rivers and the precipitation associated with warm conveyor belt ascent. Atmospheric moisture budgets calculated as cyclones pass over fixed domains relative to the cyclone tracks show that continuous evaporation of moisture in the precyclone environment moistens the feeder airstream. Evaporation behind the cold front acts to moisten the atmosphere in the wake of the cyclone passage, potentially preconditioning the environment for subsequent cyclone development.


### 1. Introduction

Intense extratropical cyclones are a major weather hazard in the midlatitudes. They can cause huge economic losses due to heavy precipitation and flooding (e.g., Pfahl and Wernli 2012; Catto and Pfahl 2013). A good understanding of the physical processes that determine the persistence of precipitation features is important for predicting precipitation totals and assessing the risk of subsequent flooding. The aim of this paper is to determine how moisture is redistributed by cyclone

airflows into regions of convergence and ascent and thus to illustrate the relationship between warm conveyor belts and atmospheric rivers.

There is some debate in the literature regarding the relationship between warm conveyor belts and atmospheric rivers. To avoid confusion in this paper, we first clarify what we understand by these terms. An atmospheric river is a long, narrow, and transient corridor of strong horizontal water vapor transport (Ralph et al. 2017). They are identified using a threshold of vertically integrated vapor transport (IVT) and are typically located ahead of the cold front in extratropical cyclones, where both the specific humidity and horizontal wind speeds are relatively large throughout the depth of the lower troposphere. A warm conveyor belt is a cyclone-relative airflow that ascends from within the boundary

---

 Denotes content that is immediately available upon publication as open access.

---

*Corresponding author:* H. F. Dacre, h.f.dacre@reading.ac.uk

DOI: 10.1175/JHM-D-18-0175.1

© 2019 American Meteorological Society. For information regarding reuse of this content and general copyright information, consult the [AMS Copyright Policy](#) ([www.ametsoc.org/PUBSReuseLicenses](http://www.ametsoc.org/PUBSReuseLicenses)).

layer to the upper troposphere along a vertically sloping isentropic surface (Carlson 1980). Since, in the absence of nonconservative forces, air parcels travel along isentropic surfaces, Harrold (1973), Browning and Roberts (1994), and others identify the warm conveyor belt airflow using cyclone-relative streamlines on a warm wet-bulb potential temperature surface. Cyclone-relative isentropic streamlines are lines tangential to the instantaneous cyclone-relative velocity of air parcels at every point on an isentropic surface. At low levels these streamlines are typically located ahead of the cold front, in the warm sector of an extratropical cyclone. The warm conveyor belt airstream then ascends from the top of the boundary layer to the upper-troposphere along the vertically sloping isentropic surface. Cyclone-relative isentropic streamlines can also be used to represent trajectories, assuming that the vertical velocity of the isentropic surface is small. Therefore, Wernli (1997), Madonna et al. (2014), and others alternatively define the warm conveyor belt as a set of trajectories that meet a criterion based on net ascent (e.g., a pressure decrease exceeding 600 hPa in the vicinity of cyclones).

Unlike an atmospheric river, a warm conveyor belt is not an Earth-relative airflow but a cyclone-relative airflow. That is, warm conveyor belts are defined in a frame of reference that moves with the cyclone. This makes it difficult to define the relationship between atmospheric rivers and warm conveyor belts. Spatial overlap between atmospheric rivers and warm conveyor belt features often exists (Knippertz et al. 2018). However, it is also possible for atmospheric rivers to exist without the presence of cyclone airflows because an atmospheric river can remain quasi-stationary while the cyclone airflows travel with the poleward propagating cyclone. It is also possible for new cyclones to form in the presence of a preexisting atmospheric river, at which time the atmospheric river can be enhanced by the new cyclone airflows. In the literature it is often stated that the moist air in an atmospheric river feeds directly into the warm conveyor belt airstream (Ralph et al. 2004; Neiman et al. 2008). However, this can only occur if the cyclone propagation velocity is equal to or slower than the pre-cold-front wind velocities, which is often not the case for developing cyclones.

Dacre et al. (2015) analyzed 200 North Atlantic cyclones and their associated moisture budgets in a cyclone-relative frame of reference. They showed that moisture flux convergence along the cold front was due to the cold front sweeping up moisture in the cyclones' warm sector. Since the cyclone typically propagates faster than the background flow field during the cyclones developing stage (Hoskins and Hodges 2002), this moisture can actually be transported away from the cyclone center.

They hypothesized that this export results in filaments of high total column water vapor (TCWV) being left behind as cyclones travel poleward from the subtropics, thus atmospheric rivers represent the footprint of a cyclone's path. In this paper we test this hypothesis by quantitatively evaluating the relationship between extratropical cyclone precipitation, IVT, and background moisture fields.

The degree to which surface fluxes affect cyclone evolution and precipitation is likely to depend on the location and timing of these fluxes relative to the cyclone passage. For example, Vanni re et al. (2017) showed that low-level temperature gradients in the atmosphere are restored rapidly by the strong surface fluxes in the cold sector of cyclones. Reed and Albright (1986) also hypothesized that large moisture fluxes in the precyclone environment could precondition the near-surface environment and lead to explosive deepening of cyclones. In idealized baroclinic life cycle experiments, Boutle et al. (2011) showed that moisture evaporated from the sea surface ahead of their cyclones was transported within the boundary layer, supplying moisture to the base of the warm conveyor belt airflow. This rearward traveling airflow is consistent with that described in Houze et al. (1976), Hoskins and West (1979), Carlson (1980), McBean and Stewart (1991), and Browning and Roberts (1994), who found that the moist low-level inflow originates in relatively easterly flow at low latitudes with air turning northward to flow approximately parallel to the cold front. In this paper we will reexamine this low-level cyclone airflow and establish its relationship to local surface fluxes in order to determine the contribution of local moisture sources to the poleward transport of moisture.

## 2. Method

### *a. Cyclone identification and compositing*

Following Dacre et al. (2012), we identify and track the position of the 200 most intense cyclones in 20 years of the ERA-Interim dataset (1989–2009) using the tracking algorithm of Hodges (1995). Tracks are identified using 6-hourly 850-hPa relative vorticity, truncated to T42 resolution to emphasize the synoptic scales. The 850-hPa relative vorticity features are filtered to remove stationary or short-lived features that are not associated with extratropical cyclones. The 200 most intense, in terms of the T42 vorticity, winter cyclone tracks with maximum intensity in the North Atlantic (70°–10°W, 30°–90°N) are used in this study. The required fields are extracted from the ERA-Interim dataset along the tracks of the selected cyclones within a 15° radius surrounding the cyclone center. For example, Fig. 1a shows the 925-hPa wind velocity

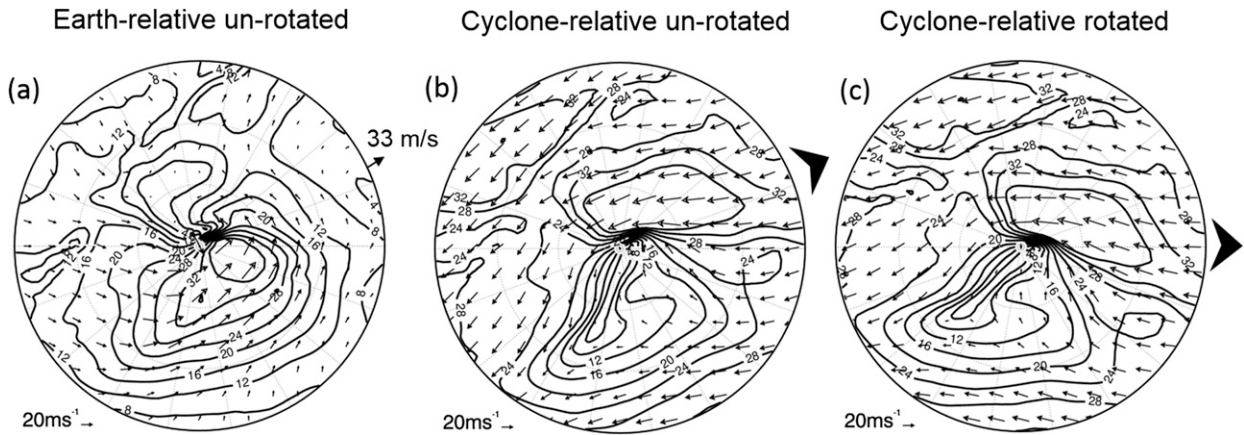


FIG. 1. Cyclone-centered 925-hPa wind speed for an individual cyclone, overlaid with wind vectors. (a) Earth-relative wind, (b) cyclone-relative wind, (c) rotated cyclone-relative wind. The cyclone propagation velocity is shown in (a). The cyclone propagation direction before and after rotation is shown in (b) and (c), respectively.

field for a randomly chosen cyclone. The cyclone-relative wind velocity field for this cyclone at this time is calculated by subtracting the cyclone propagation velocity from the Earth-relative wind, as shown in Fig. 1b. Following Catto et al. (2010), the fields are rotated according to the direction of travel of each cyclone such that the direction of travel becomes the same for all cyclones (Fig. 1c). The composites are produced by identifying the required offset time relative to the time of maximum intensity of each cyclone and the corresponding fields on the radial grid averaged over all cyclones. For the remainder of this paper the time of maximum intensity is denoted max, and times 24 and 48 h prior to maximum intensity are denoted max -24 and max -48, respectively. Since the cyclones have quite different propagation directions, performing the rotation ensures that mesoscale features such as warm and cold fronts are approximately aligned and so not smoothed out by the compositing. As this method assumes that the cyclones all intensify and decay at the same rate only the 200 most intense cyclones are included in the composite. Limiting the number of cyclones produces a more homogeneous group in terms of their evolution but will bias the mean fields to be typical of the most intense cyclones.

*b. Sensitivity to moisture sources*

The extent to which the background moisture contributes to the cyclone’s precipitation and domain integrated IVT totals is quantified by calculating the sensitivity of a cyclone’s domain integrated total precipitation (TP) and IVT at a given time to the 10-day bandpass filtered TCWV field 24h earlier (hereafter background TCWV). The filtered TCWV field represents the background moisture availability rather than

the moisture field influenced by the presence of the cyclone itself. The sensitivity is calculated at all grid points within 15° of the cyclone center yielding two-dimensional sensitivity maps. Following the ensemble sensitivity method of Garcies and Homar (2009) and Dacre and Gray (2013) a linear regression is calculated at each spatial grid point (*i, j*), between the values of the response function *J<sub>ij</sub>* (here we use TP or IVT) and the difference *x* of the precursor field (here we use background TCWV) from its mean value over all 200 cyclones. This yields a regression coefficient for the slope *m<sub>ij</sub>* given by

$$m_{ij} = \left( \frac{\partial J}{\partial x} \right)_{ij} \tag{1}$$

The linear regression uses normalized TCWV, TP, and IVT (calculated by subtracting the mean and dividing by the standard deviation), which gives a dimensionless slope. This slope *m<sub>ij</sub>* is multiplied by the standard deviation  $\sigma_{ij}$  of the background TCWV field at each grid point to give the sensitivity *S<sub>ij</sub>*:

$$S_{ij} = m_{ij} \sigma_{ij} \tag{2}$$

Multiplication of the regression coefficient by the standard deviation means that the units of *S<sub>ij</sub>* are the same as those of TP ( $\text{kg m}^{-2}$ ) and IVT ( $\text{kg m}^{-1} \text{s}^{-1}$ ), respectively. The resulting sensitivity at a grid point can then be interpreted as the change in TP or IVT associated with a one standard deviation increase in the background TCWV field at that grid point. Here TP and IVT are described as being sensitive to the background TCWV, but note that mathematically only an association is found and the inference of sensitivity relies on a postulated dynamical mechanism.

We use the false detection rate (FDR) method proposed by Wilks (2016) to test for statistical significance. The method limits the number of false null hypothesis rejections in an ensemble of statistical significance tests by reducing the critical  $p$  value used to reject an individual null hypothesis [see Wilks (2016) for a validation of this method]. The method determines the new critical  $p$  value ( $p_{\text{FDR}}$ ) by first placing all  $p$  values in ascending order and then setting  $p_{\text{FDR}}$  to the largest  $p$  value that satisfies the inequality  $p_n \leq n\alpha/N$ , where  $\alpha$ , which is set to 0.1 in this study, is the statistical significance level,  $p_n$  is the  $n$ th smallest  $p$  value, and  $N$  is the total number of hypothesis tests. Note that  $p_{\text{FDR}} = \alpha$  when  $n = N$ , hence  $p_{\text{FDR}}$  reduces to  $p_\alpha$  for a single hypothesis test. All  $p$  values less than  $p_{\text{FDR}}$  are considered to be statistically significant and are stippled in white.

### c. Eulerian moisture budgets

To quantify the importance of local surface moisture fluxes to the poleward transport of moisture we calculate Eulerian moisture budgets for 4 days in fixed domains as the cyclones pass overhead. The domains correspond to positions along to the cyclone tracks. For example, for a given cyclone position at max  $-48$ , the budget is calculated in a fixed domain of  $15^\circ$  radius centered at that position. The budget time series is centered on the time that the cyclone center is coincident with the center of the fixed domain, thus allowing us to evaluate changes in the budget as cyclones pass overhead. The budgets for all cyclones are then composited at different stages of the cyclone evolution. This is important as the balance of terms in the cyclone-relative moisture budgets evolve as the cyclones develop (Dacre et al. 2015). Note that the cyclones will evolve as they travel across the fixed domains.

Figure 2 shows the fluxes of moisture into/out of the domain. We define  $F_{\text{in}}$  as the flux of moisture into the domain and  $F_{\text{out}}$  as the flux of moisture out of the domain. Therefore,  $F_{\text{in}} > F_{\text{out}}$  implies convergence of moisture flux into the domain and  $F_{\text{in}} < F_{\text{out}}$  implies divergence of moisture out of the domain. The vertical flux of moisture into the domain from the surface, evaporation  $E$ , is split into two components; one component of the evaporation  $P_m$  is converted into local precipitation and the other component of the evaporation  $E_a$  contributes to the flux of moisture through the domain. Thus, the vertical flux of moisture out of the domain at the surface, precipitation  $P$ , also consists of two components:  $P_m$ , which as explained above comes from moisture evaporated locally, and  $P_a$ , which comes from the moisture flux into the domain. The method used to calculate the flux components of  $E$  and  $P$  are described in the appendix.

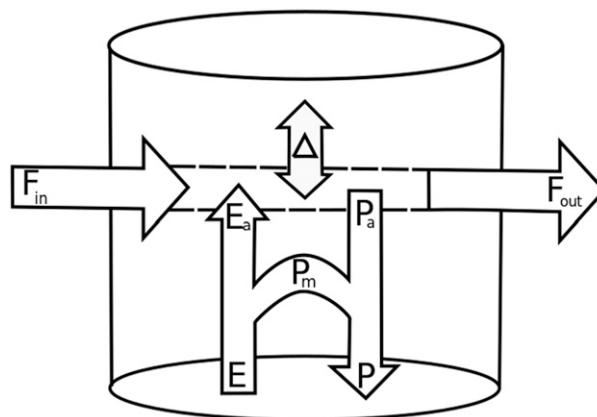


FIG. 2. Schematic of horizontal and vertical moisture fluxes into and out of a fixed cylindrical domain [adapted from Brubaker et al. (1993), their Fig. 1]. Here,  $F_{\text{in}}$  is the flux of moisture into the domain, and  $F_{\text{out}}$  is the flux of moisture out of the domain. The vertical flux of moisture into the domain from the surface, evaporation  $E$ , is split into two components; one component of the evaporation  $P_m$  is converted into local precipitation and the other component of the evaporation  $E_a$  contributes to the flux of moisture through the domain. The vertical flux of moisture out of the domain at the surface, precipitation  $P$ , consists of two components; one component of the precipitation  $P_m$  comes from moisture evaporated locally, and the other component of the precipitation  $P_a$  comes from moisture transported into the domain. The  $\Delta$  is the change in the domain moisture content.

We can define the effective flux of moisture through the domain  $F_a$  as

$$F_a = F_{\text{in}} + E_a - P_a, \quad (3)$$

and the change in the domain moisture content  $\Delta$  as

$$\Delta = F_a - F_{\text{out}}. \quad (4)$$

When the total moisture flux through the domain exceeds the flux of moisture out of the domain,  $F_a > F_{\text{out}}$ , moisture is stored within the domain. Conversely, when  $F_a < F_{\text{out}}$ , moisture is transported out of the domain. Integrating  $\Delta$  over an 82-h window (the typical time taken for cyclones to pass through the domain), allows us to determine whether cyclones act to dry or moisten the local environment, where local is defined as being within 1500 km of the cyclone center.

We define the precipitation efficiency as the fraction of the moisture flux into the domain that is removed via precipitation ( $P_a/F_{\text{in}}$ ). The precipitation efficiency provides an indication of how quickly the cyclone would “dry out” if there were no local sources of moisture. The moistening efficiency ( $E_a/F_{\text{in}}$ ) provides information about the relative importance of local versus long-distance sources of moisture,

### 3. Results

#### a. Cyclone composites

To describe the basic structure and evolution of the 200 cyclones studied, we first compute horizontal and vertical composites of cyclone structure during their developing phase. In each composite field the cyclones are located at the center of the 15° radial grid and the cyclones are rotated so that they all travel from left to right.

Figure 3a shows composite cyclone-centered fields at max  $-48$ . At this early stage in the cyclones development the cyclones typically exhibit an open wave structure in the 925-hPa equivalent potential temperature. High values of TCWV ( $>20 \text{ kg m}^{-2}$ ) are confined between the surface cold and warm fronts. Maximum precipitation occurs ahead of the cyclone center above the warm front. Figure 3b shows a circular cross section taken 5.5° from the cyclone center (anticlockwise around the arrow in Fig. 3a). Moist air ( $>80\%$  relative humidity) ascends along the sloping isentropic surfaces of the warm front with maximum vertical velocities typically occurring between 700 and 500 hPa. Near the surface, the cyclone-relative wind fields produce convergence ahead of the surface cold front.

Figures 3c and 3d show composite cyclone-centered fields at max  $-24$ . In this rapidly intensifying stage of development the 925-hPa equivalent potential temperature wave has amplified and the warm sector area has decreased. The highest values of TCWV are now found in a band ahead of the surface cold front. Maximum precipitation has approximately doubled compared to 24 h earlier, and there is a region of maximum evaporation located in the cold air behind the surface cold front. At 925 hPa the cyclone-relative wind fields produce increased convergence at the cold front, compared to 24 h earlier, leading to the accumulation of moisture and the formation of the band of high TCWV (often used as a proxy for identifying atmospheric rivers).

Figures 3e and 3f show composite cyclone-centered fields at max. By this mature stage of development the 925-hPa equivalent potential temperature frontal gradients have started to weaken and the accumulated precipitation has decreased. The 925-hPa cyclone-relative wind field convergence at the cold front occurs further from the cyclone center due to frontal fracture and the band of TCWV has also decreased in magnitude.

To illustrate the 3D structure of airflows within extratropical cyclones, cyclone-relative isentropic analysis has been performed for each cyclone. Figures 4a and 4c show composite specific humidity and cyclone-relative flow along the 285-K isentropic surface at max  $-48$  and

max  $-24$ , respectively, and Fig. 4e shows composite cyclone-relative specific humidity and flow along the 275-K isentropic surface at max. A cooler isentropic surface is shown at max to illustrate the boundary layer flow, since typically the cyclones have propagated farther north by their mature stage of development. Figures 4a, 4c, and 4e show that within the warm sector the cyclone-relative airflow is easterly, at constant pressure (1000–900 hPa), and relatively moist (specific humidity  $> 5 \text{ g kg}^{-1}$ ). At the cold front, the low-level flow diverges with one branch traveling away from the cyclone center parallel to the cold front, and another branch traveling toward the cyclone center. This is consistent with the 925-hPa cyclone-relative winds shown in Figs. 3a, 3c, and 3e. This low-level cyclone airflow (referred to in this paper as the *feeder airstream*) is responsible for supplying moist air to the base of the warm conveyor belt where it then ascends, condenses into cloud, and forms precipitation. The feeder airstream is also responsible for the formation of filaments of high TCWV seen extending along the cyclone's cold front and for exporting moisture from the cyclone. The branch of the feeder airstream traveling away from the cyclone center is weaker at max compared to the developing stages of cyclone evolution as the cyclones begin to slow down as they reach their mature stage. To the west of the cyclone center a relatively dry (specific humidity  $< 3 \text{ g kg}^{-1}$ ), descending cyclone airflow also diverges when it reaches the cold front with the strongest branch turning clockwise away from the cyclone center. At low levels during the cyclone's developing phase the dry intrusion airflow and the feeder airstream form a deformation pattern, which acts to strengthen the frontal temperature gradient.

Figures 4b and 4d show the composite specific humidity and cyclone-relative flow along the 300-K isentropic surface at max  $-48$  and max  $-24$ , respectively, and Fig. 4f shows the composite specific humidity and cyclone-relative flow along the 285-K isentropic surface at max. To the south of the cyclone center, this surface is located at approximately 800 hPa sloping up to 400 hPa to the north of the cyclone. To the east of the cyclone center air ascends along this sloped surface rising to 400 hPa. The strength of this ascending cyclone airflow increases as the cyclone intensifies. This cyclone airflow, the warm conveyor belt, is responsible for transporting warm moist air from the boundary layer to the upper troposphere. A compensating descending cyclone airflow occurs to the west of the cyclone center. This cyclone airflow, the dry intrusion, transports dry air from the upper troposphere to the lower troposphere.

Despite the inherent smoothing associated with the compositing methodology, coherent airstreams have

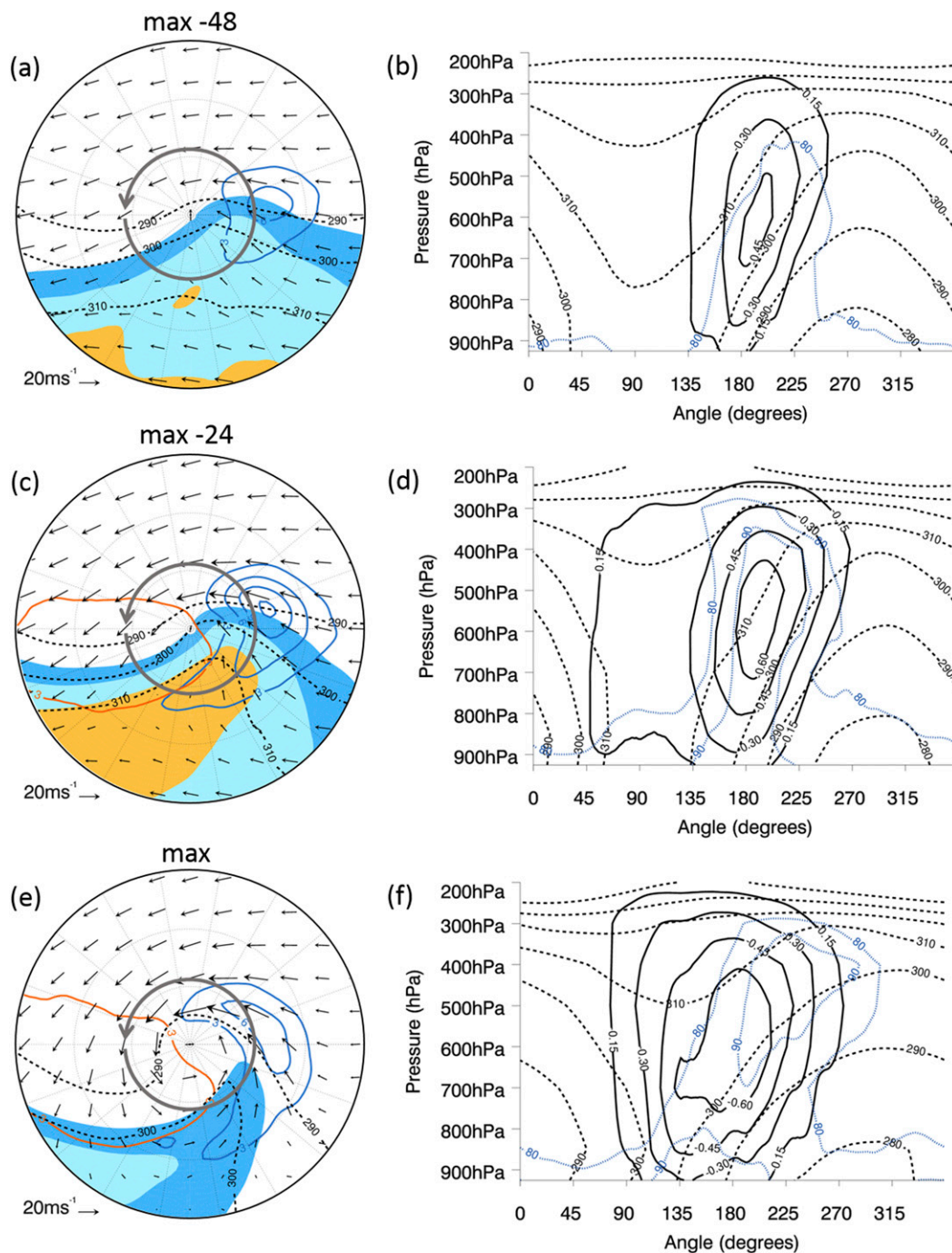


FIG. 3. Composite cyclone-centered fields at (a),(b) max  $-48$ ; (c),(d) max  $-24$ ; and (e),(f) max. (left) The 6-hourly accumulated precipitation (blue contours every 1.5 mm), 6-hourly accumulated evaporation (orange contours every 1.5 mm), TCWV (filled contours at 16, 20, and 24  $\text{kg m}^{-2}$ ), 925-hPa equivalent potential temperature (black dashed contours at 290, 300, and 310 K), and 925-hPa cyclone-relative wind vectors. Gray arrows show the location of the  $360^\circ$  vertical cross sections shown in (b), (d), and (f)  $5.5^\circ$  from the cyclone center. (right) Equivalent potential temperature (black dashed contours), omega (black solid contours at  $-1.5$ ,  $-3.0$ , and  $-4.5$   $\text{hPa s}^{-1}$ ), and relative humidity (blue dotted contours at 80% and 90%).



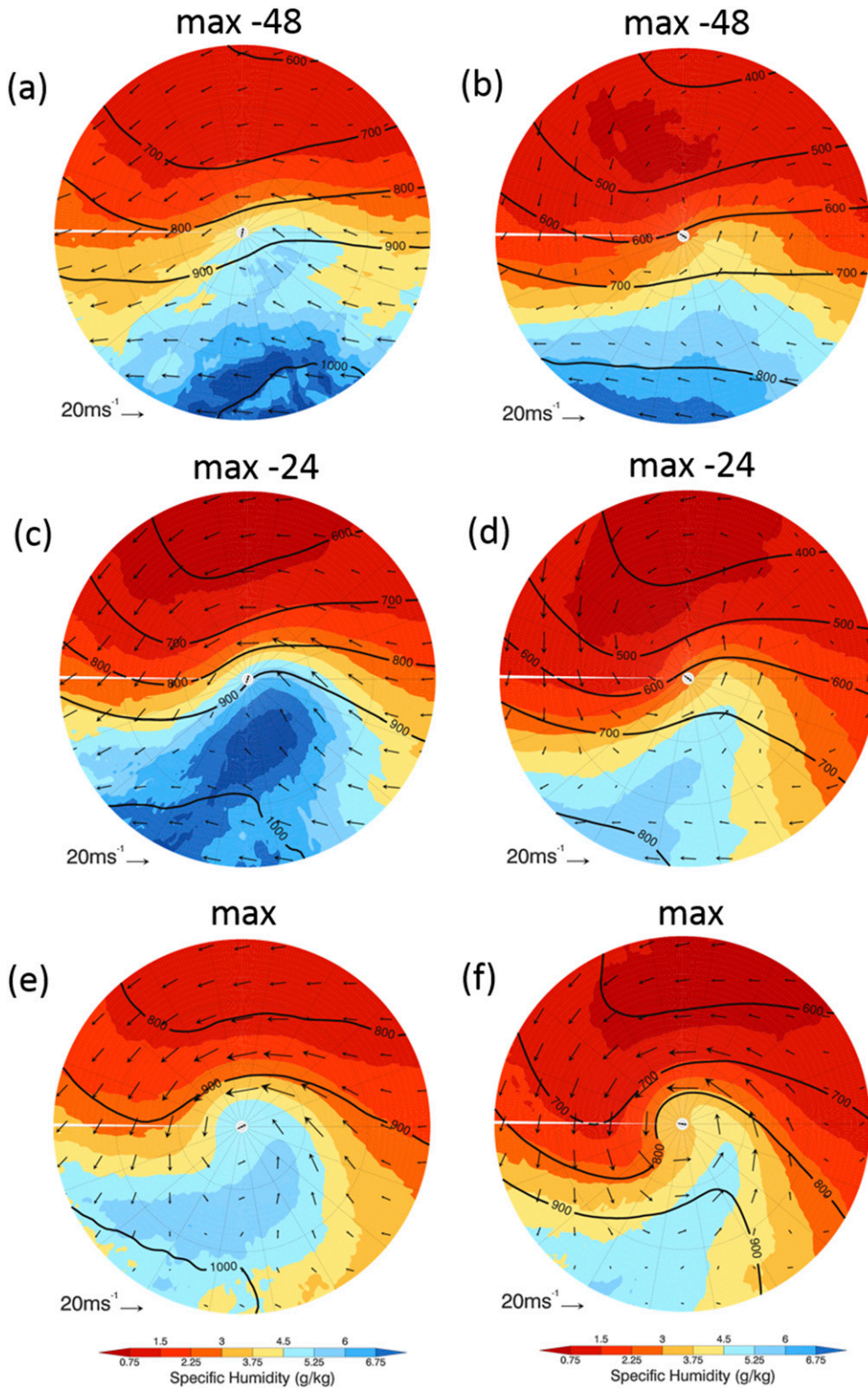


FIG. 4. Composite cyclone-centered fields at (top) max -48; (middle) max -24; and (bottom) max. (a),(c),(f) Pressure (hPa; contours), specific humidity (filled contours), and cyclone-relative flow (arrows) on the 285-K potential temperature surface. (e) Pressure, specific humidity, and cyclone-relative flow on the 275-K potential temperature surface. (b),(d) Pressure, specific humidity, and cyclone-relative flow on the 300-K potential temperature surface.

been identified in the composites. In this cyclone-relative framework, it is found that as the cyclone propagates through the background moisture field, accumulation of moisture occurring along the cold front is largely responsible for creating the band of high TCWV. The extent to which the background moisture contributes to the cyclone's domain integrated TP and IVT is the focus of the next section.

### *b. Sensitivity to background moisture*

In this section we investigate the sensitivity of a cyclone's TP and IVT to the background TCWV field 24 h earlier by performing lagged linear regression. [Figures 5a and 5c](#) show the composite background TCWV at max  $-48$  for 117 cyclones. This is a subset of the total 200 cyclones, since only 117 cyclones have a track that extends 48 h back from their time of maximum intensity. The composite background TCWV field shows a meridional gradient of TCWV with high values ( $>17 \text{ kg m}^{-2}$ ) to the south and low values ( $<8 \text{ kg m}^{-2}$ ) to the north. The orientation of the contours is fairly zonal as typically the cyclone propagate eastward during this early stage in their development and the cyclones are developing in a region where the climatological TCWV contours are also zonal (not shown). [Figures 5b and 5d](#) show the background TCWV at max  $-24$  for the 181 cyclones that have a track that extends 24 h back from their time of maximum intensity. The meridional gradient is similar to that 24 h earlier, but the orientation of the contours is not as zonal as typically the cyclones propagate in a more northeastward direction as they reach their mature stage, and the cyclones are typically developing in a region where the climatological TCWV contours are tilted southwest–northeast.

[Figure 5a](#) also shows the sensitivity of TP at max  $-24$  to the background TCWV field 24 h earlier. The maximum sensitivities are found to the right of the cyclone center (in the precyclone environment). The sensitivity is such that enhanced background TCWV in this precyclone region is associated with cyclones that precipitate more 24 h later. An increase of one standard deviation in background TCWV leads to an increase in total precipitation of up to  $0.75 \text{ kg m}^{-2}$  (approximately 12% increase in the mean TP). Therefore cyclones that propagate into regions with higher TCWV are more likely to produce more precipitation than cyclones that propagate into dry regions. [Figure 5b](#) shows the sensitivity of TP at max to the background TCWV field at max  $-24$ . As for the developing cyclones, the maximum sensitivity is found in the precyclone environment suggesting that cyclones' precipitation is controlled by the background moisture content downstream not upstream. At this mature stage of their evolution however, the

sensitivity is weaker and located farther from the cyclone center. This is likely due to the fact that both the TP and feeder airstream wind speeds reduce between max  $-24$  and max ([Figs. 4c and 4e](#), respectively).

Comparing [Figs. 5a and 5b](#) with the composite cyclone-relative flow fields at max  $-48$  and max  $-24$ , respectively ([Figs. 3a and 3c](#)), the region of maximum sensitivity is located in a region where the 925-hPa cyclone-relative winds are easterly and approximately  $15\text{--}20 \text{ m s}^{-1}$ . Thus, assuming a constant cyclone propagation velocity, it will take approximately 21–28 h for the center of the cyclone to reach the region of maximum sensitivity, that is, the background moisture in the precyclone environment is swept up by the propagating cyclone and converted into precipitation due to rapid ascent in the warm conveyor belt. Since the cyclone-relative flow into the cyclone center at low levels is from the precyclone environment we conclude that the moisture advected into the region from tropical/subtropical latitudes does not play an important role in the formation of high TP. Of course, we have only examined very intense, oceanic cyclones, and this conclusion will be tested for other subsets of cyclones as part of future work.

[Figure 5c](#) shows the sensitivity of domain integrated IVT at max  $-24$  to the background TCWV field 24 h earlier. Significant sensitivities are again found in the warm sector region of the cyclone, with maximum sensitivity in the bottom-right quadrant [similar to the TP sensitivity maximum ([Fig. 5a](#))]. Thus, enhanced background TCWV in the precyclone region is associated with cyclones with higher IVT 24 h later. An increase of one standard deviation in background TCWV leads to an increase in total precipitation of up to  $150 \text{ kg m}^{-1} \text{ s}^{-1}$  (approximately 20% increase in the mean domain integrated IVT). Therefore, cyclones that propagate into regions with higher TCWV are more likely to have stronger IVT. There is also some significant sensitivity to background TCWV in the postcyclone environment (bottom-left quadrant). This sensitivity is approximately one-third as large as that in the precyclone environment and is likely to be due to high spatial correlations in the TCWV field since the composite mean winds in this region are directed away from the cyclone center.

Finally, [Fig. 5d](#) shows the sensitivity of domain integrated IVT at max to the background TCWV field at max  $-24$ . At this mature stage of the cyclones' evolution, the sensitivity is located downstream from the cyclone center only. This is likely to be due to the fact that the structure of the cyclone evolves between max  $-24$  and max. Many of the cyclones undergo frontal fracture, with the cold front moving away from the cyclone

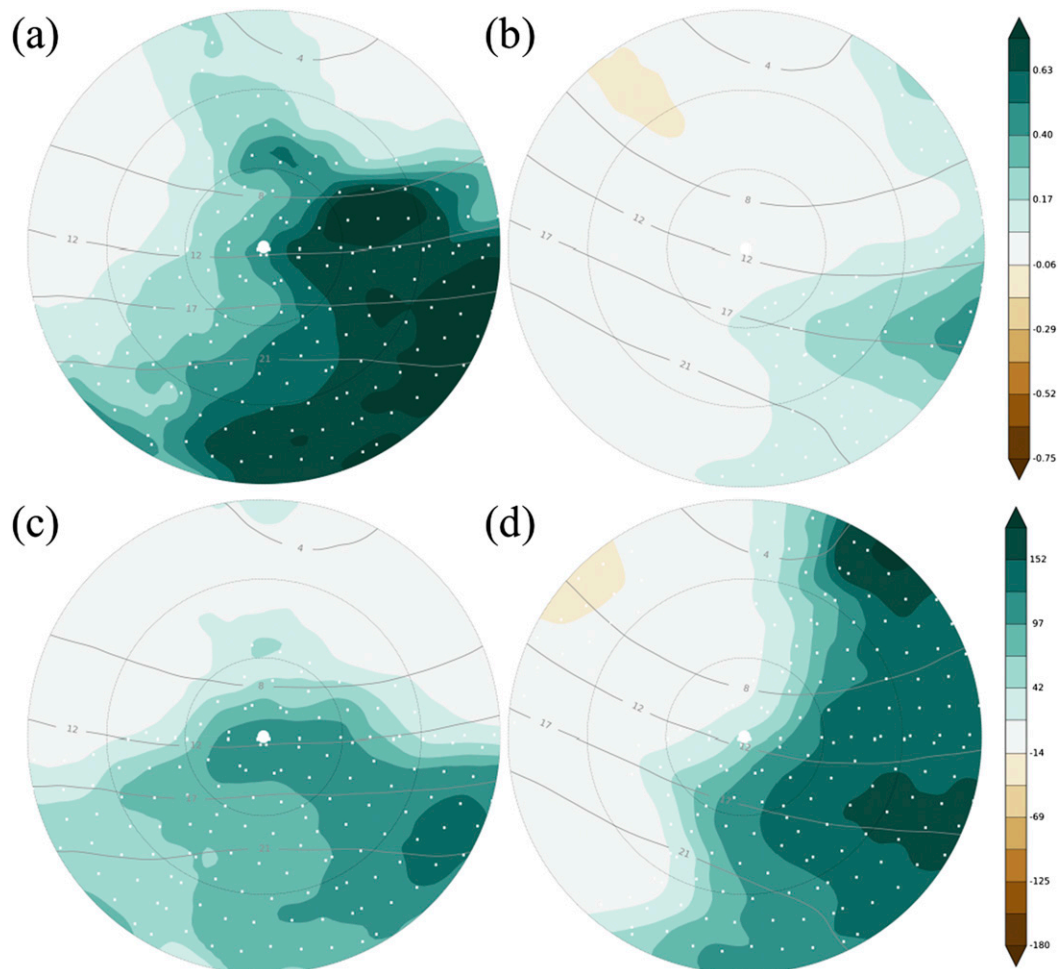


FIG. 5. Cyclone sensitivity fields (shaded; stippling denotes statistically significant sensitivities), overlaid with composite background TCWV (gray contours). (a) Sensitivity of TP at max  $-24$  to the background TCWV at max  $-48$ . (b) Sensitivity of TP at max to the background TCWV at max  $-24$ . A sensitivity value of  $0.5 \text{ kg m}^{-2}$  signifies that for one standard deviation increase in the background TCWV there is a corresponding increase in TP of  $0.5 \text{ kg m}^{-2}$ . (c) Sensitivity of domain integrated IVT at max  $-24$  to the background TCWV at max  $-48$ . (d) Sensitivity of domain integrated IVT at max to the background TCWV at max  $-24$ . A sensitivity value of  $100 \text{ kg m}^{-1} \text{ s}^{-1}$  signifies that for one standard deviation increase in the background TCWV there is a corresponding increase in total IVT of  $100 \text{ kg m}^{-1} \text{ s}^{-1}$ .

center, perpendicular to the warm front (Fig. 3e). Since the region of sensitivity is likely to be bounded by the cold front (i.e., air does not travel across the frontal boundary), this results in a region of sensitivity that is confined to the bottom-right quadrant of the domain at max, but which can extend into the bottom-left quadrant at max  $-24$ . We do not have a proposed dynamical explanation for high sensitivity in this region since they are not consistent with the magnitude and direction of the isentropic moisture fluxes shown in Fig. 4. Regions of statistically significant sensitivities exist outside the area shown. However, it is likely that these occur due to high spatial correlations in the background TCWV field shown in Fig. 4.

In summary, maximum sensitivity values are found in the precyclone environment for both TP and IVT and during the developing and mature phases of cyclone evolution. This suggests that the same mechanism is responsible for creating cyclones with higher TP and IVT. We combine this statistical sensitivity with our composite analysis of cyclones to infer that the magnitude of TCWV at the entrance of the feeder airstream is important for determining TP and IVT at a later stage in the cyclone evolution. This relationship occurs because the background moisture in the precyclone environment is swept up by the propagating cyclone and is either converted into precipitation in the warm conveyor belt or converged into a band of

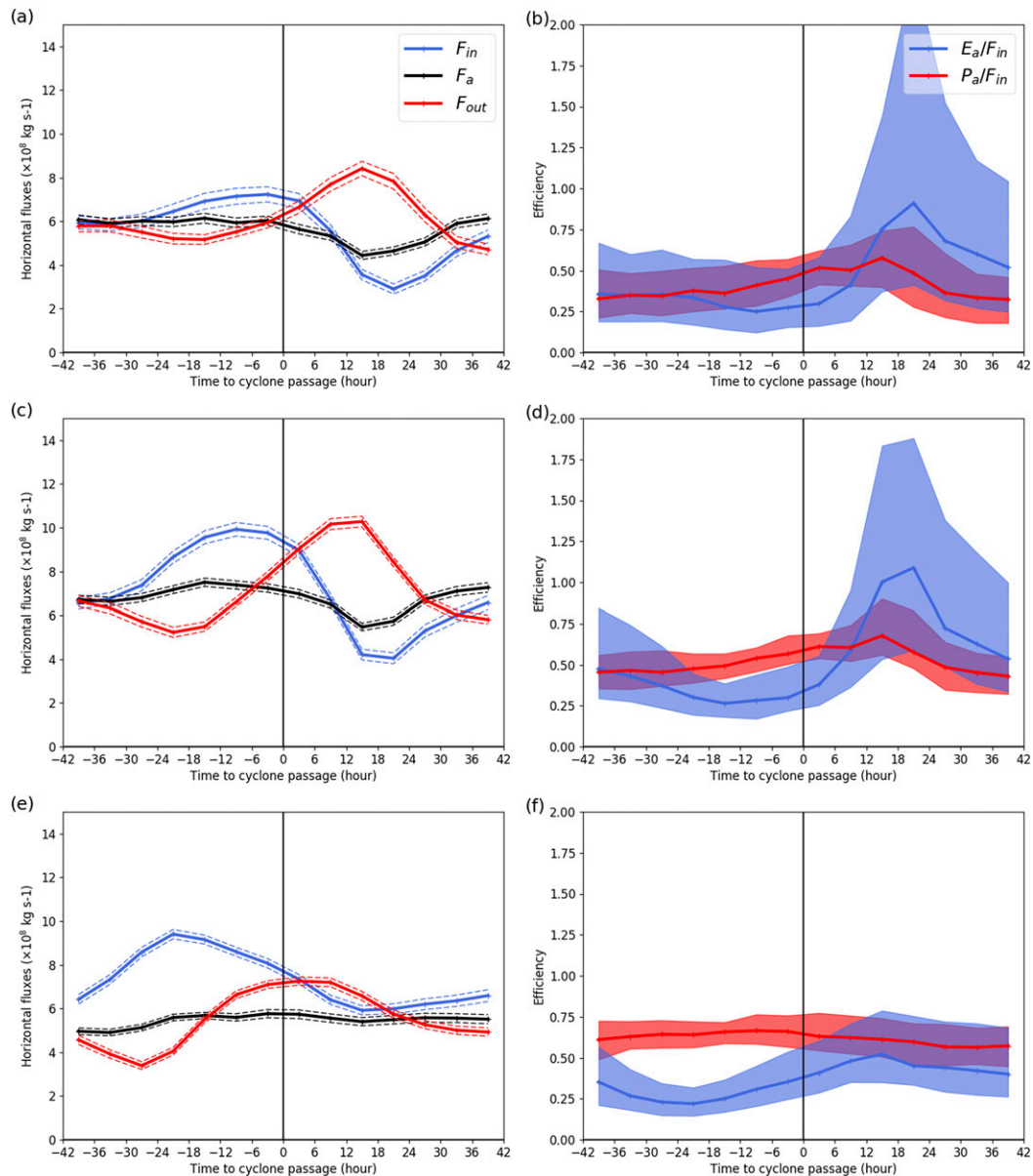


FIG. 6. (left) Horizontal fluxes and (right) precipitation efficiency ( $P_a/F_{in}$ ) and moistening efficiency ( $E_a/F_{in}$ ) over domains corresponding to cyclone positions at (a),(b) max  $-48$ , (c),(d) max  $-24$ , and (e),(f) max. Horizontal fluxes are shown as the mean (solid) and standard error of the mean (dashed). Precipitation and moistening efficiency are shown as the median (solid) and interquartile range (shading), over the following numbers of cyclones: 109 in (a) and (b); 147 in (c) and (d); and 175 in (e) and (f).

high TCWV and left behind as the cyclone propagates poleward.

### c. Eulerian moisture budgets

In this section we aim to quantify the relative contributions of horizontal and surface moisture fluxes to the overall moisture transport by the cyclones.

Figure 6a shows the composite Eulerian moisture fluxes for 109 cyclones as they travel across the domains

corresponding to their positions at max  $-48$ . This is a subset of the 117 cyclones shown Figs. 5a and 5c since cyclones tracks must extend a further 6 h forwards and backward in time. Prior to the cyclones entering the domain (from  $-42$  to  $-36$  h) convergence into the domain is negligible ( $F_{in} \simeq F_{out}$ ) and the local rate of change of moisture in the domain is also negligible ( $F_a \simeq F_{out}$ ) since evaporation  $E_a$  and precipitation  $P_a$  are approximately balanced. As the cyclones enter the

domain (from  $-30$  to  $0$  h) moisture flux convergence is positive ( $F_{in} > F_{out}$ ) due to the horizontal flux of moisture into the domain by the propagating cyclone. However the rate of change of moisture in the domain is smaller than the total due to moisture flux convergence because much of the moisture transported into the domain is removed via precipitation. For example, at  $-12$  h, on average 50% of the horizontal moisture transported into the domain is removed via precipitation ( $P_a/F_{in} \approx 0.5$ ; Fig. 6b). This loss of moisture is offset by local evaporation ( $E_a/F_{in} \approx 0.3$ ) ensuring that the cyclones do not dry out quickly. As the cyclone exits the domain (from  $+6$  to  $+30$  h), moisture flux convergence is negative ( $F_{in} < F_{out}$ ). At the same time, evaporation in the domain increases, largely due to enhanced evaporation behind the cyclone cold front (Fig. 3c). At  $+24$  h, the average moistening efficiency (70%) exceeds the precipitation efficiency (45%) (Fig. 6b), although it should be noted that the variability in moistening efficiency between cyclones is large at this point. This moisture is transported out of the domain and moistens the atmosphere in the wake of the cyclone, potentially preconditioning it for subsequent cyclone development. Over the entire cyclone passage the moisture transported away from the local environment is on average  $-13$  Pg (where  $1 \text{ Pg} = 1 \times 10^{15} \text{ g}$ ), calculated by integrating  $\Delta$  over an 82-h window. Thus, in the early stage of the cyclone development the cyclone can be said to “store” moisture that is evaporated locally and transport it poleward as it travels. Within the boundary layer this transport is slower than the cyclone propagation velocity (Fig. 4a) so while the moisture transport remains poleward, relative to the cyclone center it is left behind.

Figure 6c shows the composite Eulerian moisture fluxes for 147 cyclones as they travel across the domains corresponding to their positions at max  $-24$ . This is a subset of the 181 cyclones shown Figs. 5b and 5d since cyclones tracks must extend a further 6 h forwards and backward in time. As the cyclones enter the domain (from  $-36$  to  $0$  h) the moisture flux convergence is positive ( $F_{in} > F_{out}$ ). The moisture flux convergence is greater than 24 h earlier due to the increased moisture stored within the cyclones themselves. On average between 45% and 60% of this moisture is lost via precipitation (Fig. 6d). This loss is offset by local evaporation (moistening efficiency  $\approx 30\%$ ). Thus, there is a continuous cycle of evaporation and moisture flux convergence in the vicinity of cyclones which acts to replenish the water vapor lost via precipitation. The resulting moisture is stored within the domain ( $F_a > F_{out}$ ). As the cyclones leave the domain the situation is reversed. Moisture is transported out of the domain and transported poleward by the propagating cyclone. The moisture transported

away from the local environment is on average  $-11$  Pg, thus the cyclone continues to pull in moisture from the local environment and transports it poleward.

Figure 6e shows the Eulerian horizontal moisture fluxes for 175 cyclones as they travel across the domains corresponding to their positions at max. Unlike the early and intensifying stages of cyclone life cycle, the precipitation and evaporation fluxes ( $E_a$  and  $P_a$ ) do not balance initially. The precipitation efficiency is on average  $>60\%$  at  $-42$  h whereas the moistening efficiency is on average  $<40\%$ . At this mature stage of the cyclone development the evaporation in the domain is not large enough to replenish the moisture lost via precipitation and as a result the cyclones rapidly dry out. Thus, the moisture diverging out of the domain is significantly smaller than that entering the domain for almost the entire time period. The moisture transported away from the local environment is smaller than during the developing and intensifying stages of the cyclone life cycle ( $-1$  Pg). Therefore, in the mature stage of the cyclone development the cyclone “empties” of moisture and the poleward transport of moisture decreases as the cyclone begins to decay.

In summary, since precipitation and moistening efficiencies are nonzero we can conclude that, even if  $F_{in} = F_{out}$ , the same moisture that enters the domain does not leave the domain. That is, moisture lost via precipitation is replenished by a combination of local evaporation and moisture from the local environment (where local is within 1500 km of the cyclone center). As a result the local environment is drier following the passage of a cyclone during its developing and mature stages. The contribution of local evaporation to the horizontal moisture flux is calculated using  $E_a/F_{in}$  averaged over the developing stages of cyclone evolution (max  $-48$  and max  $-24$ ). Between  $-42$  and  $0$  h local evaporation contributes approximately 30% to the horizontal moisture flux, providing a continuous source of moisture to the feeder airstream airflow in the precyclone environment. Between  $0$  and  $+42$  h local evaporation contributes approximately 70% to the horizontal moisture flux in the postcyclone environment (although the variability between cyclones is large), potentially preconditioning it for subsequent cyclone development.

#### 4. Discussion and conclusions

Figure 7 shows a schematic of the cyclone-relative airflows and their relation to Eulerian features such as the surface fronts and regions of high precipitation and TCWV. The feeder airstream is a low-level flow of moist air that travels rearwards, relative to the cyclone propagation direction. At the cold front the feeder airstream

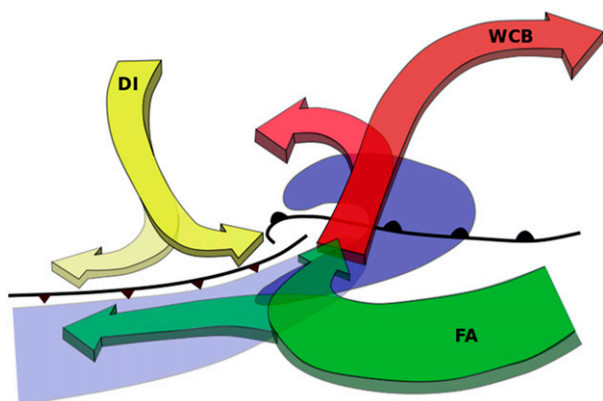


FIG. 7. Schematic of cyclone-relative airflows overlaid on cyclone surface features. Cold and warm front (black), precipitation (dark blue shading), and high TCWV (light blue shading). Ascending warm conveyor belt (WCB; red), split into lower cyclonically turning and higher anticyclonically turning branch. Low-level rearward flowing feeder airstream (FA; green), split into lower cyclonically turning and higher anticyclonically turning branch. Descending dry intrusion (DI; yellow), split into lower anticyclonically turning branch and higher cyclonically turning branch.

velocity decreases resulting in accumulation of moisture and the formation of a band of high TCWV. One branch of the feeder airstream turns toward the cyclone center. This branch is responsible for transporting moist air to the base of the warm conveyor belt where it then rises up over the warm front, leading to cloud and precipitation formation. This flow is consistent with that described in Houze et al. (1976), Carlson (1980), McBean and Stewart (1991), and Browning and Roberts (1994), who found that moist low-level cyclone inflow originates in relatively easterly flow at low latitudes with air turning northward to flow approximately parallel to the cold front. The sensitivity analysis has shown that cyclone precipitation totals at a given time are sensitive to the moisture content at the entrance to the feeder airstream 24 h earlier, that is, the more moisture that is transported to the base of the warm conveyor belt by the feeder airstream, the higher the cyclone's precipitation. The lower branch of the feeder airstream turns away from the cyclone center and travels parallel to the cold front. At low levels, wind speeds are slower than the propagation velocity of the cyclone, which travels with a velocity at the steering level ( $\approx 700$  hPa) resulting in the export of moisture from the cyclone. The moisture in this branch of the feeder airstream is left behind by the poleward traveling cyclone and, over time, results in a long filament of high TCWV marking the track of the cyclone (or cyclone footprint). This is consistent with the trajectory analysis shown in Hoskins and West (1979). The sensitivity analysis has also shown that cyclone IVT totals at a given time are also sensitive to the moisture

content at the entrance to the feeder airstream 24 h earlier, that is, the more moisture that is swept up by the cold front as it travels poleward through the atmosphere, the stronger the atmospheric river. Thus, the feeder airstream cyclone airflow explains the link between flooding and atmospheric rivers observed by Ralph et al. (2006), Lavers et al. (2011), Lavers et al. (2012), and others. Evaporation in the precyclone environment ensures that there is a continuous reservoir of moisture available to the feeder airstream allowing both persistent precipitation features and continuous filaments of high TCWV (atmospheric rivers) to form.

Behind the cyclone a dry airflow, known as the dry intrusion, descends from mid- and upper levels toward the surface cold front. At the cold front it is forced to diverge and flow both toward and away from the cyclone center parallel to the cold front. Moisture evaporated from the surface behind the cold front due to cold dry air transported over a warm moist surface is largely exported from the cyclone although some moisture can be transported into the center of the cyclone during the mature stage of cyclone evolution at midlevels where it contributes to precipitation formation. The moisture evaporated behind the cold front acts to moisten the atmosphere in the wake of the cyclone passage. This, in combination with the feeder airstream, potentially helps to precondition the environment for subsequent cyclone development.

*Acknowledgments.* O.M-A.'s contribution was funded by the United Kingdom's Natural Environment Research Council (NERC) as part of the National Centre for Atmospheric Sciences. Cheikh MBengue was funded by a NERC Grant (NE/M005909/1) Summer: Testing Influences and Mechanisms for Europe (SummerTIME). The ERA-Interim data were obtained freely from <http://apps.ecmwf.int/datasets/>. Information on how to obtain the cyclone identification and tracking algorithm can be found from <http://www.nerc-essc.ac.uk/~kih/TRACK/Track.html>. Any additional data may be obtained from [h.f.dacre@reading.ac.uk](mailto:h.f.dacre@reading.ac.uk). We thank Kevin Hodges for providing his ETC tracking code, Nigel Roberts, Sue Gray, and Peter Clark for helpful discussions on this work. We also thank three anonymous reviewers for their helpful comments, which improved the manuscript.

## APPENDIX

### Calculation of Horizontal Fluxes

The average horizontal flux through the domain  $F = \int \mathbf{Q} \cdot \hat{\mathbf{n}} dl$ , where  $\mathbf{Q}$  is the domain-averaged vertically IVT and  $\hat{\mathbf{n}}$  is a unit vector normal to the domain's horizontal projection's circumference. The integral is

computed over half of this circumference to find  $F = 2rQ$ , where  $Q$  is the magnitude of  $\mathbf{Q}$  and  $r$  is the domain's radius. Following Trenberth (1999) (see also Brubaker et al. 1993),

$$F = \frac{1}{2}(F_{in} + F_{out}). \tag{A1}$$

Furthermore, the domain-integrated moisture flux convergence  $C = F_{in} - F_{out}$ . Thus,  $F_{in} = F + C/2$  and  $F_{out} = F - C/2$ .

The change in the domain's moisture content  $\Delta$  is given by

$$\Delta = F_{in} - F_{out} + E - P. \tag{A2}$$

We assume that precipitation can be split into two parts, one due to moisture flux into the domain  $P_a$ , and another due to local evaporation converted into precipitation  $P_m$ , that is,

$$P = P_a + P_m. \tag{A3}$$

Using (A2) and (A3) to rewrite (A1), we get

$$F = F_{in} + \frac{1}{2}(E - P_m - P_a) - \frac{1}{2}\Delta, \tag{A4}$$

which can also be split into two parts, one due to the moisture flux into the domain  $Q_a = F_{in} - 1/2P_a - 1/2\Delta$ , and another due to evaporated moisture  $Q_m = 1/2(E - P_m)$ . Following Brubaker et al. (1993) and Trenberth (1999), we assume that the ratio  $P_a/P_m$  is equal to the ratio  $Q_a/Q_m$ , from which we find that

$$\frac{P_a}{P_m} = \frac{2F_{in} - \Delta}{E}. \tag{A5}$$

Using (A4) and (A5) in (A3) yields

$$P_m = P \left( \frac{E}{2F + P} \right). \tag{A6}$$

REFERENCES

Boutle, I., S. Belcher, and R. Plant, 2011: Moisture transport in midlatitude cyclones. *Quart. J. Roy. Meteor. Soc.*, **137**, 360–373, <https://doi.org/10.1002/qj.783>.  
 Browning, K., and N. Roberts, 1994: Structure of a frontal cyclone. *Quart. J. Roy. Meteor. Soc.*, **120**, 1535–1557, <https://doi.org/10.1002/qj.49712052006>.  
 Brubaker, K. L., D. Entekhabi, and P. Eagleson, 1993: Estimation of continental precipitation recycling. *J. Climate*, **6**, 1077–1089, [https://doi.org/10.1175/1520-0442\(1993\)006<1077:EOCPR>2.0.CO;2](https://doi.org/10.1175/1520-0442(1993)006<1077:EOCPR>2.0.CO;2).  
 Carlson, T. N., 1980: Airflow through midlatitude cyclones and the comma cloud pattern. *Mon. Wea. Rev.*, **108**, 1498–1509,

[https://doi.org/10.1175/1520-0493\(1980\)108<1498:ATMCAT>2.0.CO;2](https://doi.org/10.1175/1520-0493(1980)108<1498:ATMCAT>2.0.CO;2).  
 Catto, J. L., and S. Pfahl, 2013: The importance of fronts for extreme precipitation. *J. Geophys. Res. Atmos.*, **118**, 10 791–10 801, <https://doi.org/10.1002/jgrd.50852>.  
 —, L. C. Shaffrey, and K. I. Hodges, 2010: Can climate models capture the structure of extratropical cyclones? *J. Climate*, **23**, 1621–1635, <https://doi.org/10.1175/2009JCLI3318.1>.  
 Dacre, H. F., and S. L. Gray, 2013: Quantifying the climatological relationship between extratropical cyclone intensity and atmospheric precursors. *Geophys. Res. Lett.*, **40**, 2322–2327, <https://doi.org/10.1002/grl.50105>.  
 —, M. Hawcroft, M. Stringer, and K. Hodges, 2012: An extratropical cyclone atlas: A tool for illustrating cyclone structure and evolution characteristics. *Bull. Amer. Meteor. Soc.*, **93**, 1497–1502, <https://doi.org/10.1175/BAMS-D-11-00164.1>.  
 —, P. A. Clark, O. Martinez-Alvarado, M. A. Stringer, and D. A. Lavers, 2015: How do atmospheric rivers form? *Bull. Amer. Meteor. Soc.*, **96**, 1243–1255, <https://doi.org/10.1175/BAMS-D-14-00031.1>.  
 Garcies, L., and V. Homar, 2009: Ensemble sensitivities of the real atmosphere: application to Mediterranean intense cyclones. *Tellus*, **61A**, 394–406, <https://doi.org/10.1111/j.1600-0870.2009.00392.x>.  
 Harrold, T., 1973: Mechanisms influencing the distribution of precipitation within baroclinic disturbances. *Quart. J. Roy. Meteor. Soc.*, **99**, 232–251, <https://doi.org/10.1002/qj.49709942003>.  
 Hodges, K., 1995: Feature tracking on the unit sphere. *Mon. Wea. Rev.*, **123**, 3458–3465, [https://doi.org/10.1175/1520-0493\(1995\)123<3458:FTOTUS>2.0.CO;2](https://doi.org/10.1175/1520-0493(1995)123<3458:FTOTUS>2.0.CO;2).  
 Hoskins, B. J., and N. V. West, 1979: Baroclinic waves and frontogenesis. Part II: Uniform potential vorticity jet flows-cold and warm fronts. *J. Atmos. Sci.*, **36**, 1663–1680, [https://doi.org/10.1175/1520-0469\(1979\)036<1663:BWAFPI>2.0.CO;2](https://doi.org/10.1175/1520-0469(1979)036<1663:BWAFPI>2.0.CO;2).  
 —, and K. I. Hodges, 2002: New perspectives on the Northern Hemisphere winter storm tracks. *J. Atmos. Sci.*, **59**, 1041–1061, [https://doi.org/10.1175/1520-0469\(2002\)059<1041:NPOTNH>2.0.CO;2](https://doi.org/10.1175/1520-0469(2002)059<1041:NPOTNH>2.0.CO;2).  
 Houze, R. A., Jr., J. D. Locatelli, and P. V. Hobbs, 1976: Dynamics and cloud microphysics of the rainbands in an occluded frontal system. *J. Atmos. Sci.*, **33**, 1921–1936, [https://doi.org/10.1175/1520-0469\(1976\)033<1921:DACMOT>2.0.CO;2](https://doi.org/10.1175/1520-0469(1976)033<1921:DACMOT>2.0.CO;2).  
 Knippertz, P., F. Pantillon, and A. H. Fink, 2018: The devil in the detail of storms. *Environ. Res. Lett.*, **13**, 044002, <https://doi.org/10.1088/1748-9326/aabd3e>.  
 Lavers, D. A., R. P. Allan, E. F. Wood, G. Villarini, D. J. Brayshaw, and A. J. Wade, 2011: Winter floods in Britain are connected to atmospheric rivers. *Geophys. Res. Lett.*, **38**, L23803, <https://doi.org/10.1029/2011GL049783>.  
 —, G. Villarini, R. P. Allan, E. F. Wood, and A. J. Wade, 2012: The detection of atmospheric rivers in atmospheric reanalyses and their links to British winter floods and the large-scale climatic circulation. *J. Geophys. Res.*, **117**, D20106, <https://doi.org/10.1029/2012JD018027>.  
 Madonna, E., H. Wernli, H. Joos, and O. Martius, 2014: Warm conveyor belts in the ERA-Interim dataset (1979–2010). Part I: Climatology and potential vorticity evolution. *J. Climate*, **27**, 3–26, <https://doi.org/10.1175/JCLI-D-12-00720.1>.  
 McBean, G. A., and R. E. Stewart, 1991: Structure of a frontal system over the northeast Pacific Ocean. *Mon. Wea. Rev.*, **119**, 997–1013, [https://doi.org/10.1175/1520-0493\(1991\)119<0997:SOAFSO>2.0.CO;2](https://doi.org/10.1175/1520-0493(1991)119<0997:SOAFSO>2.0.CO;2).  
 Neiman, P. J., F. M. Ralph, G. A. Wick, J. D. Lundquist, and M. D. Dettinger, 2008: Meteorological characteristics and overland

- precipitation impacts of atmospheric rivers affecting the west coast of North America based on eight years of SSM/I satellite observations. *J. Hydrometeor.*, **9**, 22–47, <https://doi.org/10.1175/2007JHM855.1>.
- Pfahl, S., and H. Wernli, 2012: Quantifying the relevance of cyclones for precipitation extremes. *J. Climate*, **25**, 6770–6780, <https://doi.org/10.1175/JCLI-D-11-00705.1>.
- Ralph, F. M., P. J. Neiman, and G. A. Wick, 2004: Satellite and CALJET aircraft observations of atmospheric rivers over the eastern North Pacific Ocean during the winter of 1997/98. *Mon. Wea. Rev.*, **132**, 1721–1745, [https://doi.org/10.1175/1520-0493\(2004\)132<1721:SACAOO>2.0.CO;2](https://doi.org/10.1175/1520-0493(2004)132<1721:SACAOO>2.0.CO;2).
- , —, —, S. I. Gutman, M. D. Dettinger, D. R. Cayan, and A. B. White, 2006: Flooding on California's Russian River: Role of atmospheric rivers. *Geophys. Res. Lett.*, **33**, L13801, <https://doi.org/10.1029/2006GL026689>.
- , and Coauthors, 2017: Atmospheric rivers emerge as a global science and applications focus. *Bull. Amer. Meteor. Soc.*, **98**, 1969–1973, <https://doi.org/10.1175/BAMS-D-16-0262.1>.
- Reed, R. J., and M. D. Albright, 1986: A case study of explosive cyclogenesis in the eastern Pacific. *Mon. Wea. Rev.*, **114**, 2297–2319, [https://doi.org/10.1175/1520-0493\(1986\)114<2297:ACSOEC>2.0.CO;2](https://doi.org/10.1175/1520-0493(1986)114<2297:ACSOEC>2.0.CO;2).
- Trenberth, K. E., 1999: Atmospheric moisture recycling: Role of advection and local evaporation. *J. Climate*, **12**, 1368–1381, [https://doi.org/10.1175/1520-0442\(1999\)012<1368:AMRROA>2.0.CO;2](https://doi.org/10.1175/1520-0442(1999)012<1368:AMRROA>2.0.CO;2).
- Vanni re, B., A. Czaja, and H. F. Dacre, 2017: Contribution of the cold sector of extratropical cyclones to mean state features over the Gulf Stream in winter. *Quart. J. Roy. Meteor. Soc.*, **143**, 1990–2000, <https://doi.org/10.1002/qj.3058>.
- Wernli, H., 1997: A Lagrangian-based analysis of extratropical cyclones. II: A detailed case-study. *Quart. J. Roy. Meteor. Soc.*, **123**, 1677–1706, <https://doi.org/10.1002/qj.49712354211>.
- Wilks, D. S., 2016: “The stippling shows statistically significant grid points”: How research results are routinely overstated and overinterpreted, and what to do about it. *Bull. Amer. Meteor. Soc.*, **97**, 2263–2273, <https://doi.org/10.1175/BAMS-D-15-00267.1>.